Nuclear Instruments and Methods in Physics Research B 366 (2016) 198–205

Contents lists available at ScienceDirect

Nuclear Instruments and Methods in Physics Research B

journal homepage: www.elsevier.com/locate/nimb

Involvement of crystallinity in various luminescent bands in yttrium aluminate

Takaaki Morimoto [a,*], Masayuki Harima [a], Yosuke Horii [a], Yoshimichi Ohki [a,b,*]

[a] Department of Electrical Engineering and Bioscience, Waseda University, Shinjuku, Tokyo 169-8555, Japan
[b] Research Institute for Materials Science and Technology, Waseda University, Shinjuku, Tokyo 169-8555, Japan

ARTICLE INFO

Article history:
Received 3 June 2015
Received in revised form 11 October 2015
Accepted 31 October 2015
Available online 18 November 2015

Keywords:
$YAlO_3$
Ion implantation
Photoluminescence
Crystallinity

ABSTRACT

When single crystal $YAlO_3$ was implanted with P^+ or B^+ ions, optical absorption increases significantly at energies slightly lower than the band gap energy, indicating that localized electronic states were induced. Furthermore, the ion implantation decreases the intensity of an X-ray diffraction peak and changes its position randomly, which indicates that the crystalline structure of the sample was deformed. The intensities of photoluminescence (PL) bands due to impurities of Cr^{3+} and Er^{3+} and those originating in self-trapped excitons and antisites become smaller or disappear after the ion implantation. On the other hand, the intensity of the PL due to oxygen vacancies does not change. Such contrasting effects of the sample's crystallinity on the luminescence intensity are explained by the different manners of involvement of the crystal structure in the luminescence mechanism among these PLs in $YAlO_3$.

1. Introduction

Various photoluminescence (PL) bands appear in yttrium aluminate ($YAlO_3$) perovskite crystal. It is known that point defects such as impurities and vacancies are deeply involved in these PLs. It is also known that the existing forms of impurities or vacancies in inorganic crystals are closely related to the crystallinity of the mother crystal. Several PLs emitted from $YAlO_3$ are used for lasers [1–3] and scintillators [4–6]. For example, the PL that emits photons with the wavelength of 2.0 μm can be induced by doping Tm^{3+} and is used for lasers [1]. Furthermore, the PL at 350 nm induced by doping Ce^{3+} is used for scintillators [4–6]. Therefore, it is important to investigate the effects of the crystallinity of $YAlO_3$ on its luminescence.

On the other hand, $YAlO_3$ is one of the promising candidates for a gate insulator in advanced metal oxide semiconductor field-effect transistors (MOSFETs) for large scale integration and power conversion circuits, since it has a high relative permittivity (~16) [7] and a wide band gap energy (E_g: 7.9 eV) [8]. However, $YAlO_3$ is not used practically as gate insulators, since it contains point defects abundantly. Therefore, investigation on the nature of the defects is important. Regarding this, the authors have proved that measurements of PL bands and analysis of their behavior can provide many pieces of valuable information on point defects in various inorganic insulating materials [9–24].

In other words, behavior of PL can provide important clues not only to the study of luminescent phenomena themselves for lasers or scintillators but also to the study of insulating properties of $YAlO_3$. From these backgrounds, in this research, the crystallinity of $YAlO_3$ was changed by ion implantation in order to investigate its involvement in the properties of various PL bands. Furthermore, PL characteristics observed in the present $YAlO_3$ are compared with those in $LaAlO_3$ and YSZ reported in the authors' preceding papers [23,24].

2. Experimental procedures

The samples examined are $YAlO_3$(100) single crystals grown by the Czochralski method in a German company, Crystal GmbH. They were cut to rectangular plates with a thickness of 0.5 mm. The plates were implanted with positive phosphorus (P^+) or boron (B^+) ions at a fluence of 1.0×10^{15} cm^{-2} with an acceleration energy of 100 keV using an ion accelerator (Ulvac, UP-150) in Waseda University.

Before and after the ion implantation, X-ray diffraction (XRD) patterns were obtained in the in-plane mode, which is suitable for analyzing the sample surface, with Cu Kα X-rays at room temperature using a Rigaku Rint-Ultima III. Furthermore, the presence of impurities in the sample before the ion implantation was

* Corrsponding authors at: Department of Electrical Engineering and Bioscience, Waseda University, Shinjuku, Tokyo 169-8555, Japan (T. Morimoto and Y. Ohki).
E-mail addresses: takaaki.morimoto@akane.waseda.jp (T. Morimoto), yohki@waseda.jp (Y. Ohki).

http://dx.doi.org/10.1016/j.nimb.2015.10.072
0168-583X/

measured by inductively coupled plasma mass spectrometry (ICP-MS) with an Agilent 7700x. In addition, electron spin resonance (ESR) spectra were obtained at the X-band frequency of 9.20 GHz with a microwave power of 2.00 mW at room temperature using a JEOL JES-FA 300. Here, the magnetic field was applied parallel to the principal axis of the sample plate.

In order to measure PL excitation and emission spectra and optical absorption spectra, synchrotron radiation (SR, beam energy: 750 MeV) at the BL3B line in UVSOR Facility at the Institute for Molecular Science, Okazaki, Japan was used as a photon source. The absorption was measured at 10 K using a 2.5 m off-plane Eagle-type normal incidence monochromator and a photodiode set before and after the sample plate, respectively. When measuring PLs, a PL excitation spectrum, namely a PL intensity spectrum obtained by changing the energy of incident excitation photons, was measured first using the incidence monochromator, a 300-mm triple-grating rear monochromator (Acton, SpectraPro-300i), and a charge-coupled device (CCD) camera (Princeton Instruments) at 10 K. Then, a PL emission spectrum, or an intensity spectrum of each PL as a function of photon energy, excited by photons with the energy that can induce the strongest PL, was measured. The spectral intensity was calibrated with the intensity of excitation SR at each photon energy for both the former PL excitation spectrum and the latter PL emission spectrum.

3. Results

Fig. 1 shows the projected ranges of P^+ and B^+ ions in $YAlO_3$ estimated using a simulation program called SRIM2011 [25]. The range is estimated to be about 80 nm for the P^+ ions and 200 nm for the B^+ ions with the energy of 100 keV. Since these projected ranges are shallow, the in-plane mode was used to obtain XRD patterns. As indicated by the spectrum I shown in the inset in Fig. 2, the unimplanted sample exhibits a peak at $2\theta\chi = 34.6°$, which corresponds to the diffraction at (002) planes of crystalline $YAlO_3$ [26]. This is reasonable, since the sample had been set in a way that the (002) peak should be observed. In addition, the sample also exhibits another peak at $2\theta\chi = 74.0°$, the assignment of which is unclear due to the lack of database. Here, the authors pay attention to the clearer one at 34.6°. This peak appears at a different angle and its height decreases if the sample was implanted with the ions. To verify repeatability, XRD patterns were also observed for two more P^+-ion implanted, one more B^+-ion implanted, and three more unimplanted samples. The result is summarized in Fig. 3. Here, each peak height is normalized by the average of the peak heights observed for the four unimplanted samples. The ion implantation decreased the peak height by 30–95% and varied the peak position randomly. This is in contrast with the fact that the four unimplanted samples always exhibit the peak at the same position.

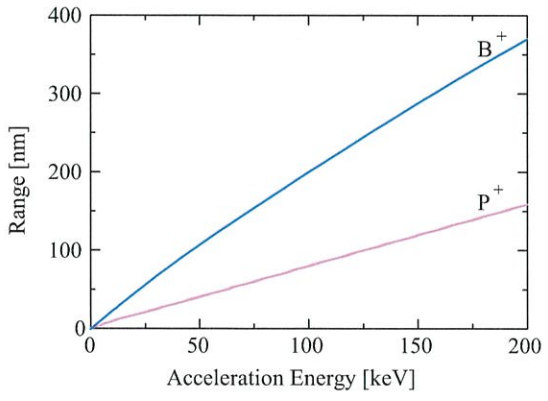

Fig. 1. (Color online.) Projected ranges of P^+ and B^+ ions in $YAlO_3$.

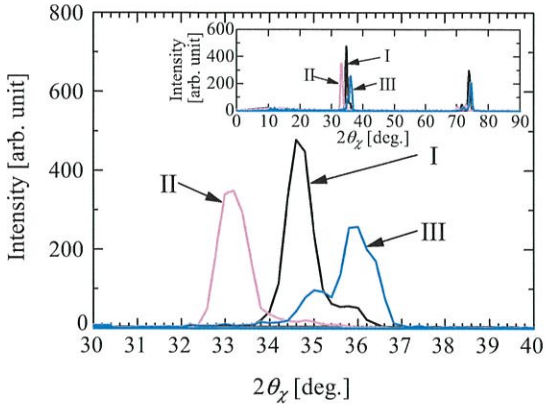

Fig. 2. (Color online.) In-plane XRD patterns observed at angles from 30° to 40°, before the ion implantation (curve I) and after the implantation of P^+ ions (II) and B^+ ions (III) at a fluence of 10^{15} cm^{-2}. Inset: whole angle patterns.

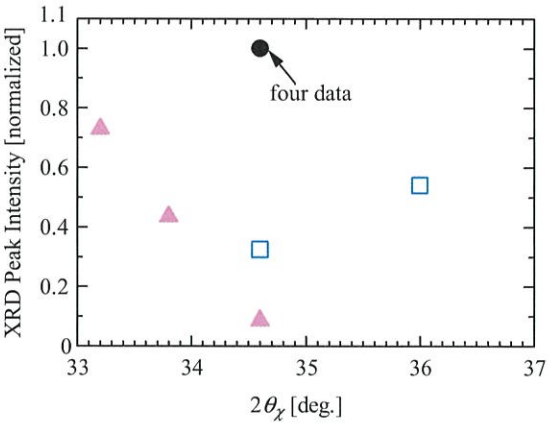

Fig. 3. (Color online.) Fluctuations in height and position of the XRD peak observed in the unimplanted (black solid circles), P^+ ion-implanted (pink (light gray in b/w) solid triangles), and B^+ ion-implanted (blue (dark gray) open squares) samples. Note that the peak intensities are normalized by their original intensities before the implantation.

Table 1 lists the averages and standard deviations of concentrations of impurities in $YAlO_3$ analyzed by ICP-MS for five samples. On average, the samples contain 20 ppm of Cr, 51 ppm of Er, and 6 ppm of Nd. Note that contamination by Fe cannot be confirmed, since the spectrometer is equipped with a Fe filament.

Fig. 4 shows PL emission spectra observed for $YAlO_3$ crystal plates at 10 K before the ion implantation in the whole photon-energy range measured in this research, namely from 1.5 to 6.0 eV. Here, the green (light gray in b/w) solid, brown (dark gray) dashed, black dashed, and violet (dark gray) solid curves represent

Table 1
Impurities in $YAlO_3$ analyzed for five samples by ICP-MS.

Elemental concentration (ppm)				
	Cr	Er	Nd	Fe
Average	20	51	6.1	<200*
Standard deviation	6.5	2.1	0.74	–

* Fe: below a method-dependent background level of 200 ppm.

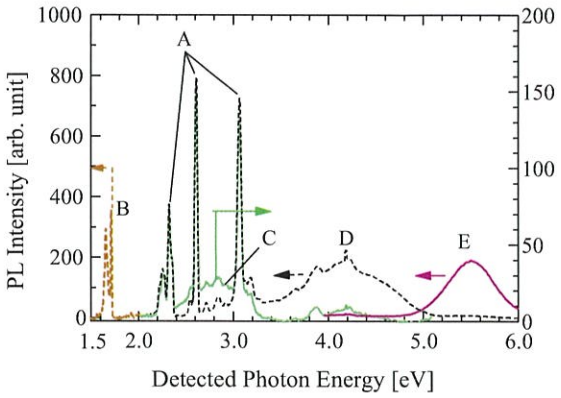

Fig. 4. (Color online.) PL emission spectra observed at 10 K before the ion implantation in the whole photon-energy range measured in this research, namely from 1.5 to 6.0 eV. Here, green (light gray in b/w) solid, brown (dark gray) dashed, black dashed, and violet (dark gray) solid curves represent PL emission spectra induced by 5.2, 6.7, 7.7, and 8.0 eV photons, respectively.

PL emission spectra induced by 5.2, 6.7, 7.7, and 8.0 eV photons, respectively. In total, five PL peaks or bands, which are called PL A to E, are seen. The excitation and emission energies of each PL are listed in the second and third columns in Table 2. Note that an enlarged figure for each PL will be found in Fig. 5. First, the presence of multi-component PL A consisting of a dual component at around 2.3 eV and two other sharp components at 2.6 and 3.1 eV is confirmed. Secondly, sharp PL B with two components at 1.66 and 1.71 eV is seen. Thirdly, there is also a very broad PL band C spreading from around 2.0 to around 3.4 eV with its maximum at around 2.8 eV. Furthermore, two very broad PL bands D and E ranging from around 3.2 to 5.0 eV with its maximum at around 4.2 eV and from around 4.8 to 6.2 eV with its maximum at around 5.5 eV are also observable.

Next, Fig. 5 shows enlarged emission spectra for each PL observed at 10 K before and after the sample had been implanted with P^+ or B^+ ions at a fluence of 10^{15} cm^{-2}. For all the spectra, black curves (I) are for the unimplanted samples and pink (light gray in b/w) ones (II) are for the P^+-implanted samples, whereas blue (dark gray) ones (III) are for the B^+-implanted samples. Fig. 5(a) shows that the multi-component PL A at around 2.3, 2.6 and 3.1 eV disappears completely, while the intensity of the very broad PL C at around 2.0–3.4 eV is unchanged by the ion implantation. The PL B in Fig. 5(b) with two components at 1.66 and 1.71 eV becomes weak by the ion implantation. As shown in Fig. 5(c), the very broad PL D with its maximum at around 4.2 eV disappears almost completely when ions were implanted. Complete disappearance of the sharp multi-component PL A can be reconfirmed in this figure. Furthermore, the broad PL E at around 5.5 eV also disappears completely by the ion implantation as shown in Fig. 5(d).

Table 2
PL bands due to point defects in $YAlO_3$.

PL	Excitation energy (eV)	Emission energy (eV)	Effect of ions	Origin of PL
A	7.5	2.3, 2.6, 3.1	Disappear	Er^{3+} [48]
B	6.5–7.0	1.66, 1.71	Decrease	Cr^{3+} [39]
C	5.2	2.0–3.4 (maximum at 2.8 eV)	No change	Oxygen vacancy [8]
D	7.5–7.7	3.2–5.0 (maximum at 4.2 eV)	Disappear	STE [43]
E	8.0	4.8–6.2 (maximum at 5.5 eV)	Disappear	Y^{3+}/Al^{3+} antisite [44]

Fig. 6 shows optical absorption spectra measured at 10 K before and after the ion implantation. The value of E_g estimated for the unimplanted plate agrees with a literature value (=7.9 eV) [8]. It is clearly shown that the implantation of either P^+ or B^+ ions increases significantly the optical absorption in an energy range slightly lower than E_g.

Fig. 7 shows PL excitation spectra measured at 10 K. Since the spectra were taken by changing the excitation photon energy manually by a step of 0.1 or 0.2 eV using the incidence monochromator, the spectra are represented by dots. Furthermore, the colors are in accordance with those in Figs. 5 and 6. Namely, the black solid circles are for the unimplanted samples and the pink (light gray in b/w) solid triangles are for the samples implanted with P^+ ions at the fluence of 10^{15} cm^{-2}, while the blue (dark gray) open squares are for the B^+-implanted samples.

According to Fig. 7(a), all the three sharp components of PL A at 2.3, 2.6 and 3.1 eV have similar or identical PL excitation spectra with a broad but clear excitation maximum at around 7.5 eV, which is slightly lower than E_g. On the other hand, in Fig. 7(b), the intensity of PL B becomes maximum at the excitation energy around 6.5–7.0 eV, which is much smaller than E_g. As shown in Fig. 7(c), PL C becomes maximum when it is excited at about 5.2 eV, which is also much smaller than E_g. Similarly to PL A, the broad PL D with its maximum at 4.2 eV shown in Fig. 7(d) has a PL excitation maximum at 7.5–7.7 eV, which is also slightly lower than E_g. Lastly, broad PL E with its maximum at around 5.5 eV seen only in the unimplanted sample exhibits a PL excitation maximum at 8.0 eV, which is very close to E_g, as shown in Fig. 7(e).

Fig. 8 shows the ESR spectrum observed in the unimplanted $YAlO_3$ crystal sample at room temperature. A clear signal with three features at 297, 320, and 352 mT is seen.

4. Discussion

4.1. Structural changes

First, the structural changes induced by the ion implantation are analyzed from the results of optical absorption and XRD measurements. The increase in optical absorption at energies slightly lower than E_g shown in Fig. 6, which was induced by the implantation with P^+ or B^+ ions, indicates that new localized electronic states were formed in the band gap by the ion implantation. On the other hand, the decrease in the XRD peak height shown in Figs. 2 and 3, which was also induced by the implantation, indicates the collapse of the crystal structure. Furthermore, the random shift of the XRD peak position shown in Fig. 3 indicates that the lattice constants were changed.

When ions are implanted in solids, the displacement of atoms and the generation of atomic vacancies are induced [27,28], as a result of the collapse of the crystal structure. Regarding this, numbers of vacancies of three different atoms Y, Al, and O, induced in $YAlO_3$ by the implantation with B^+ or P^+ ions, were calculated using the software TRIM2013 [25] on the assumption that ions were implanted at a fluence of 1.0×10^{15} cm^{-2} with an acceleration energy of 100 keV. Fig. 9 shows the results. The atomic vacancies are generated most abundantly at positions 170 and 50 nm deep under the surface by the implantation with B^+ and P^+ ions, respectively. Fig. 9 also indicates that oxygen vacancies are induced more abundantly than Y or Al vacancies, which is simply because $YAlO_3$ contains more O atoms than Y or Al atoms. The distortion of lattice planes, induced by such displacement of atoms and generation of atomic vacancies, should be responsible for the shift of the XRD peak [29,30]. The results mentioned above clearly show that the degradation of crystallinity, the distortion of lattice planes, and

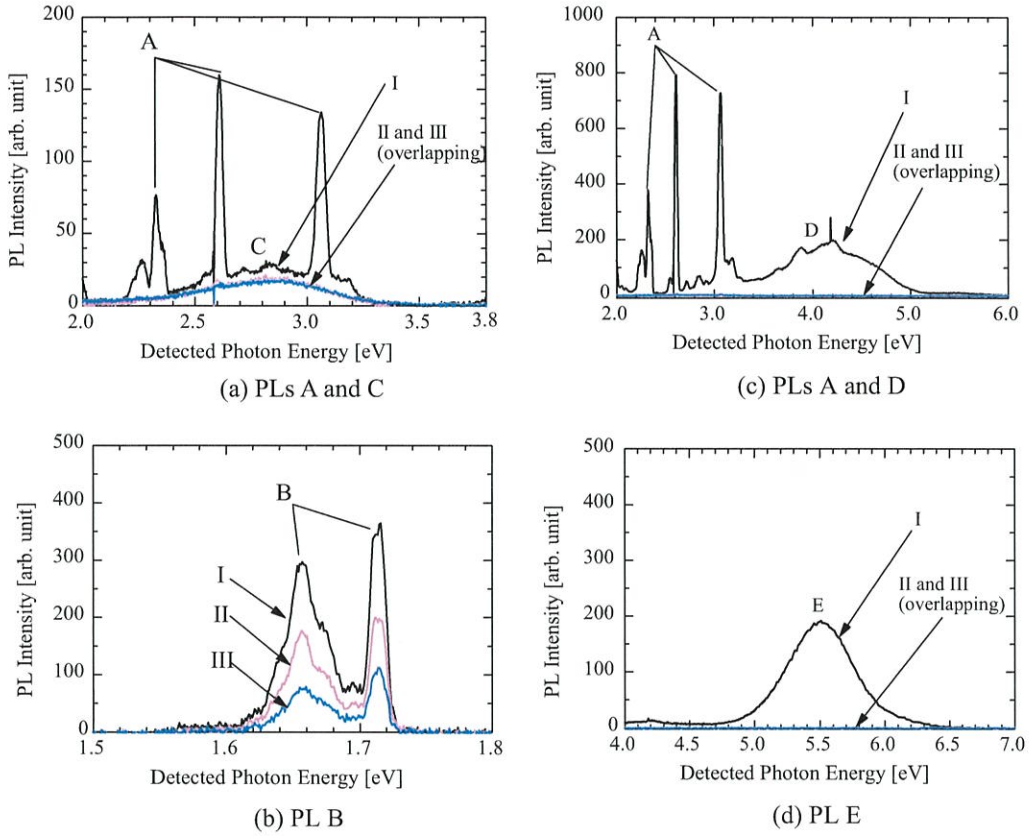

Fig. 5. (Color online.) Enlarged emission spectra for each PL observed at 10 K before and after they had been implanted with P^+ or B^+ ions at a fluence of 10^{15} cm^{-2}. For all the spectra, black curves (I) are for the unimplanted samples and pink (light gray in b/w) ones (II) are for the P^+-implanted samples, whereas blue (dark gray) ones (III) are for the B^+-implanted samples.

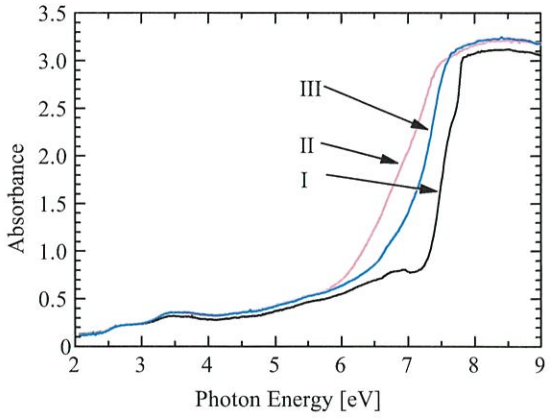

Fig. 6. (Color online.) Optical absorption spectra observed at 10 K. Curve I represents the absorption observed before ion implantation, while II and III are for the samples implanted with P^+ and B^+ ions at a fluence of 10^{15} cm^{-2}, respectively.

the generation of localized electronic states are induced by the ion implantation.

As another possible reaction induced by the ion implantation, point defects may change their charging states. If a certain PL is due to such point defects, it is reasonably assumed that the change in valence electrons should exert an unignorable influence on the PL. Namely, the energy and spectral shape of the PL emission or excitation peak would be changed if the charging state of the responsible point defect is altered. However, at least as for PLs B and C observed in the present research, their emission and excitation spectra do not exhibit any meaningful change by the ion implantation as shown in Figs. 5(a) and (b) and 7(b) and (c). This indicates that the change in charging state is not a dominant process.

Among various ion-induced phenomena, the above-mentioned change in charging state would be annealed at a low temperature compared to various structural changes such as lattice deformation and formation of atomic vacancies [28]. For example, it has been reported that an electronic damage induced in SiO_2 by ion implantation is recovered by annealing at 200 °C [28]. The authors also revealed that the change in charging state of oxygen vacancies induced in YSZ by the irradiation of ultraviolet photons is recovered by annealing at 260 °C [16]. Therefore, if the effects of annealing treatments at various temperatures are studied well, we will be able to find whether the dominant change induced by ions is electronic or structural. This will be studied in the near future. As a tentative examination, the sample was annealed at various temperatures from 500 to 1000 °C in oxygen after it had been implanted with P^+ ions at a fluence of 10^{15} cm^{-2}. As a result, it has become clear that PL B, which was decreased once by the ion implantation, only scarcely recovers its intensity by the annealing at 900 °C as shown in Fig. 10. This result indicates that the reaction influencing dominantly on the PL properties is structural.

4.2. PL excitation and emission spectra

Next, the effects of the above-mentioned structural changes of $YAlO_3$ on its PL characteristics are discussed. For that purpose,

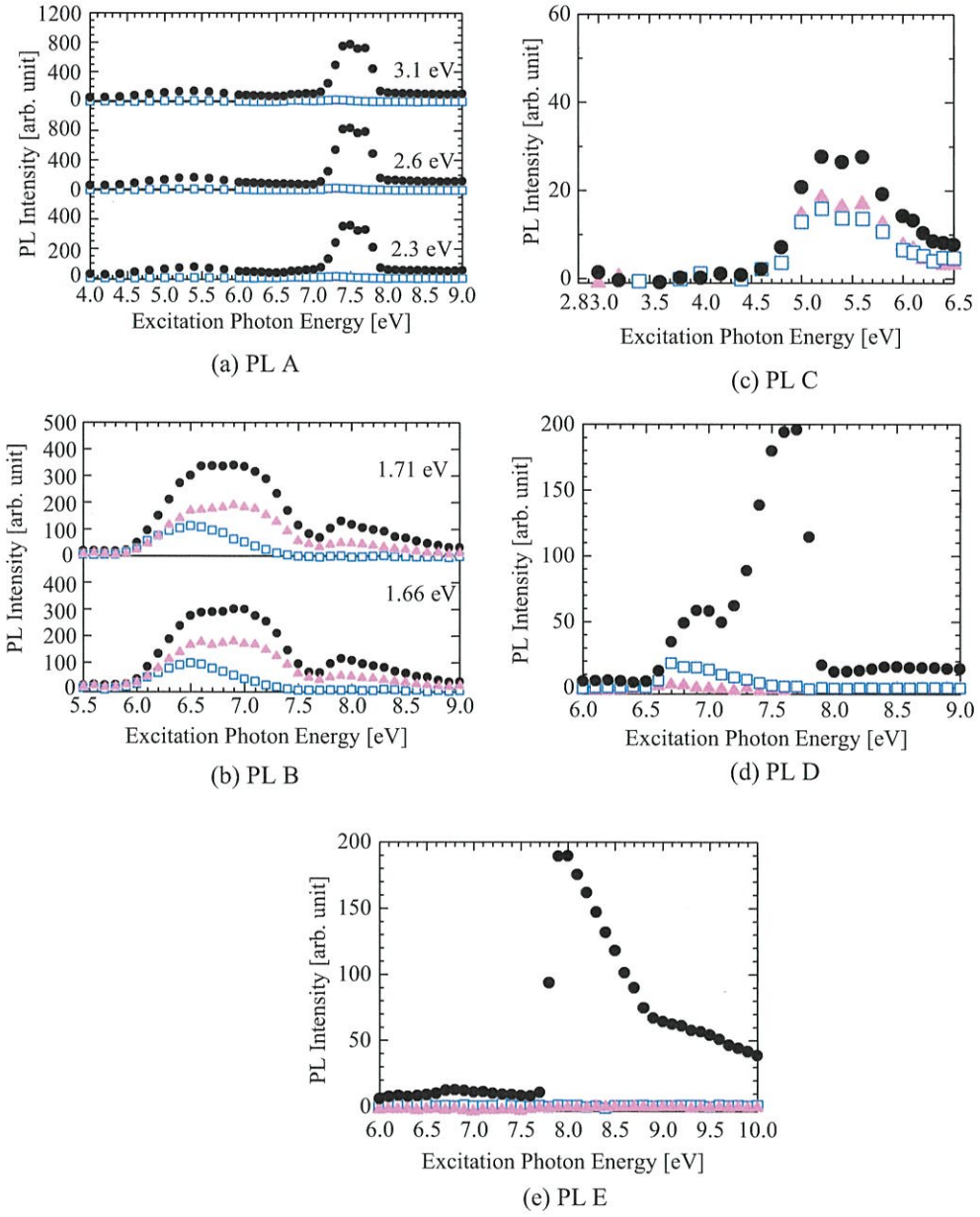

Fig. 7. (Color online.) Excitation spectra of PL A detected at 2.3, 2.6, and 3.1 eV (a), PL B detected at 1.66 and 1.71 eV (b), PL C detected at 2.8 eV (c), PL D detected at 4.2 eV (d), and PL E detected at 5.5 eV (e). Black solid circles are for the unimplanted samples and the pink (light gray in b/w) solid triangles are for the samples implanted with P^+ ions at the fluence of 10^{15} cm^{-2}, while the blue (dark gray) open squares are for the B^+-implanted samples. All spectra were measured at 10 K.

the assignment of each PL has to be known. First, the very broad PL C spreading very widely at around 2.8 eV seen in Fig. 5(a) is due to oxygen vacancies [8]. This type of PL due to oxygen vacancies is known to appear in many oxides such as SiO_2 [31–36], ZnO [37], Ta_2O_5 [38], $LaAlO_3$ [10,24], and yttria-stabilized zirconia (YSZ) [23]. It has also been known that the PL due to oxygen vacancies appears regardless of the sample's crystallinity in all these materials with the exception of YSZ [23]. Namely, the PL appears in YSZ only when its crystallinity is high. The reason for the exception of YSZ is that oxygen vacancies appear in YSZ according to the ratio of yttria to zirconia in YSZ [23]. Here, in the present $YAlO_3$, the very broad PL C due to oxygen vacancies appears almost similarly before and after the ion implantation as shown in Fig. 5(a). That is to say, the PL C is induced in $YAlO_3$ by the transition process of electrons that is not affected by its crystallinity.

Although oxygen vacancies should have been induced by the ion implantation as indicated in Fig. 9, the intensity of PL C due to oxygen vacancies is not increased by the implantation as shown in Figs. 5(a) and 7(c). When Al_2O_3 is implanted with various ions, the intensity of optical absorption due to the F^+ center, namely, the oxygen vacancy that captures one electron, starts to increase when the nuclear energy deposition reaches 10^{23} keV cm^{-3} [28]. Here, the project range of ions with an energy of 100 keV in a solid substance is around 100 nm [25]. Therefore, if the whole energy that the ions possess is given to the substance, its energy density becomes 10^{22} keV cm^{-3} at a fluence of 10^{15} cm^{-2}. Taking account of the fact that the nuclear energy deposition is a fraction of the total energy deposition, the energy of 100 keV and the fluence of 10^{15} cm^{-2}, used in the present research, are not high enough to increase the density of oxygen vacancies to a level, which yields

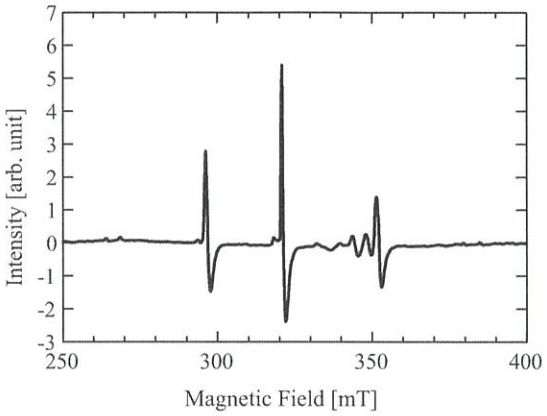

Fig. 8. (Black and white.) ESR spectrum observed in unimplanted $YAlO_3$ crystal at room temperature. The magnetic field was applied parallel to the principal axis.

an appreciable increase in PL C. For the purpose of examining whether oxygen vacancies are induced by the ion implantation in the present $YAlO_3$ samples, ESR measurements were carried out. However, no obvious increase in the signal intensity due to oxygen vacancies was detected, probably due to the fact that the ions could reach only up to 100 nm from the surface of the 0.5-mm-thick-sample.

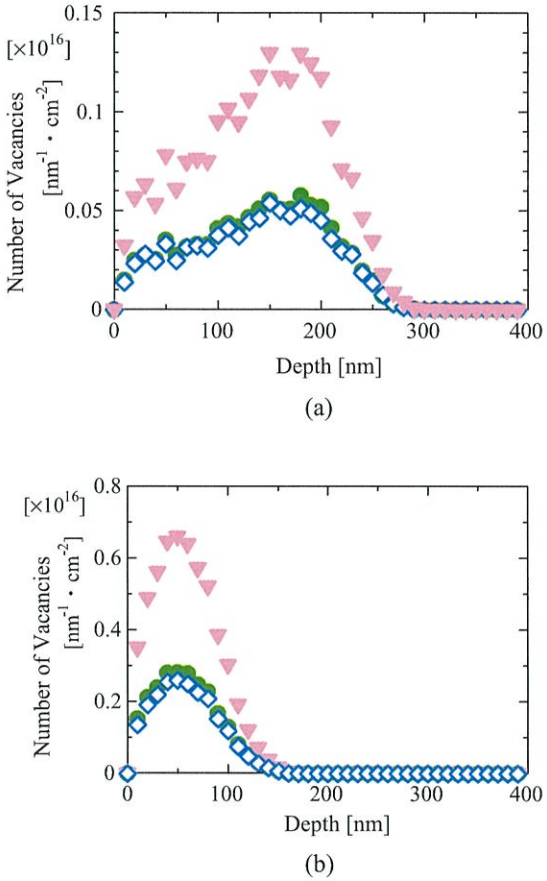

Fig. 9. (Color online.) Numbers of atomic vacancies induced by the implantation with B^+ (a) and P^+ (b) ions with an acceleration energy of 100 keV at a fluence of 1.0×10^{15} cm^{-2}, calculated using software TRIM2013. Vacancies of O, Y, and Al are denoted by pink (light gray in b/w) solid inverted triangles, blue (dark gray) open diamonds, and green (dark gray) solid circles, respectively.

Secondly, as for the sharp PL B with two components at 1.66 and 1.71 eV seen in Fig. 5(b), its spectral shape is similar to that of the R-line luminescence of Cr^{3+} in $YAlO_3$ [39]. The ICP-MS results listed in Table 1 indicate that the present $YAlO_3$ contains Cr. Furthermore, the positions of the three ESR features at 297, 320 and 352 mT shown in Fig. 8 are similar to those of the features assigned to Cr^{3+} in the literature [40]. Moreover, the presence of Cr^{3+} in single crystal $LaAlO_3$ with a similar structure to $YAlO_3$ was confirmed by ESR and also by the presence of similar R-line luminescence [10,22]. It has been reported that Cr^{3+} occupies an Al^{3+} site in an octahedral ligand field of O^{2-} when the sample is crystalline and that the ligand field resolves the degeneracy of the *d*-orbital of Cr^{3+} due to the Stark effect [41,42]. By this resolution, the R-line energy levels are formed and the PL appears. Therefore, PL B with two components at 1.66 and 1.71 eV is attributable to Cr^{3+} and it appears only when the sample's crystallinity is high. Furthermore, PL B has its excitation maximum at around 6.5–7.0 eV as shown in Fig. 7(b), which is much smaller than E_g. Therefore, the excitation of PL B is not related to an electronic transition across the bandgap.

Thirdly, the very broad PL D at 4.2 eV shown in Fig. 5(c) seems to be due to self-trapped excitons (STEs) [43]. This type of excitons were also assigned to the origin of a very similar PL in Y_2O_3 [43]. Here, STEs or excitons in general form localized electronic states just below the conduction band edge. Therefore, PL D seems to be induced by an electronic transition from such exciton states. If additional localized electronic states are induced in the forbidden band by the ion implantation as discussed in relation to Fig. 6, they will mask the exciton states. Therefore, the disappearance of the PL D at 4.2 eV after the ion implantation is reasonable. In other words, this PL appears only when the sample's crystallinity is high.

Fourthly, the PL E at 5.5 eV shown in Fig. 5(d) seems to be due to antisites where Y^{3+} substitutes for Al^{3+}, because of a marked similarity between the PLs observed in this research and reported in the literature [44]. The rising portion of the PL excitation spectrum observed in the sample before the ion implantation shown by the black circles in Fig. 7(e) is very close to that of the absorption curve observed before the ion implantation shown in Fig. 6. This indicates that the excitation of PL E is directly or indirectly related to the electronic excitation across the clear bandgap of the sample before the ion implantation. Therefore, it is reasonable that the PL E due to the antisites appears only when the sample's crystallinity is high as in the case of PL D due to STEs.

Fifthly, as for the sharp PL A with components at 2.3, 2.6 and 3.1 eV observable in Fig. 5(a) and (c), its spectral shape is similarly sharp to that of the PL B with two components at 1.66 and 1.71 eV

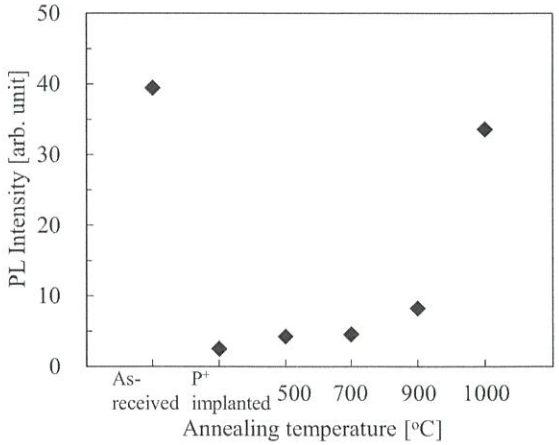

Fig. 10. (Black and white.) Effects of thermal annealing, which followed the implantation with P^+ ions, on the intensity of PL B due to Cr^{3+}.

shown in Fig. 5(b). This indicates that the origins of two PLs A and B are similar. Therefore, the origin of PL A with components at 2.3, 2.6 and 3.1 eV seems also to be a transition metal impurity like Cr^{3+}. One possible candidate would be Fe^{3+}. Although the presence of Fe could not be confirmed by ICP-MS due to the abundance of Fe in the background noise as shown in Table 1, Fe has been confirmed to exist in Al_2O_3 [45] and several aluminates such as $Y_3Al_5O_{12}$ [46] and $LaAlO_3$ [47]. In this regard, PL A could be due to Fe^{3+}. However, a more plausible candidate is a rare-earth ion. As shown in Table 1, Er and Nd exist in the present $YAlO_3$ samples. It is well known that Er^{3+} has luminescent levels capable of emitting photons of 2.33, 2.61 and 3.07 eV [48], namely exactly the same energies of the sharp components of PL A shown in Fig. 5 (a) and (c). However, Nd^{3+} does not have such levels. In this regard, Er^{3+} is the origin of the PL A.

Next, the intensities of the PLs A, B, D, and E, which are respectively due to Er^{3+}, Cr^{3+}, STEs, and antisites, disappear or become smaller by the ion implantation. On the other hand, the intensity of the PL C due to oxygen vacancies does not change. This difference in the dependence of crystallinity on the disappearance of PL is a reflection of the difference in the involvement of the sample's crystallinity in each PL. Furthermore, according to Figs. 5–7, although new localized electronic states were formed by the ion implantation, no additional PL emission and excitation bands were observed at least in the energy range from 1.5 to 10 eV, indicating that the new states are non-radiative.

Lastly, if we compare Fig. 5(a) and (c) with Fig. 5(b), we find that the effect of ion implantation on the intensity of PL A due to Er^{3+} is more obvious than that on the intensity of PL B due to Cr^{3+}. Namely, PL A due to Er^{3+} disappears completely by the ion implantation. The three components of PL A are induced by electronic transitions from an excited state ($^2P_{3/2}$) of 4*f* electrons to three lower states ($^4I_{9/2}$, $^4I_{11/2}$, and $^4I_{13/2}$) [48]. Since 4*f* orbital electrons are shielded by 5*s* orbital electrons, these transitions are hardly influenced by the crystal field. On the other hand, the excitation of the 4*f* electrons to the excited $^2P_{3/2}$ state is realized by being assisted by STE, which exists stably only when the sample is crystalline. Therefore, the excitation of PL A is influenced by the crystal field. On the other hand, as mentioned above, PL B is due to the Cr^{3+} ion that occupies the Al^{3+} site in the octahedral ligand field. Therefore, its intensity decreases if the ligand field collapses. For this reason, the effect of ion implantation differs between PLs A and B. The details of this will be reported elsewhere.

To summarize, the effects of ion implantation on all the PL bands in $YAlO_3$ are listed in the fourth column of Table 2. Furthermore, the origin of each PL, the certainty of which has been confirmed by the present research, is listed in the rightmost column.

4.3. Comparison with film samples

To confirm further whether the appearance of the sharp PL B with two components at 1.66 and 1.71 eV shown in Fig. 5(b) is limited to the samples with high crystallinities, the following experiment was carried out. Namely, using an alkoxide solution containing Y and Al (Kojundo Chemical Laboratory, AlY-05(1/1)), thin films with a thickness of approximately 100 nm were spin-coated on a Si(100) single crystal substrate. The films were thermally annealed at different temperatures between 600 and 1000 °C for 120 min in air, and in-plane XRD patterns and PL emission spectra were taken. As shown in Fig. 11, the films annealed at 600, 700 and 800 °C are amorphous, while those annealed at 900 and 1000 °C are polycrystalline containing $YAlO_3$ and $Y_3Al_5O_{12}$. This is consistent with the fact that $YAlO_3$ and $Y_3Al_5O_{12}$ in a film deposited by a sol–gel method start to crystallize at approximately 1000 and 900 °C, respectively [49].

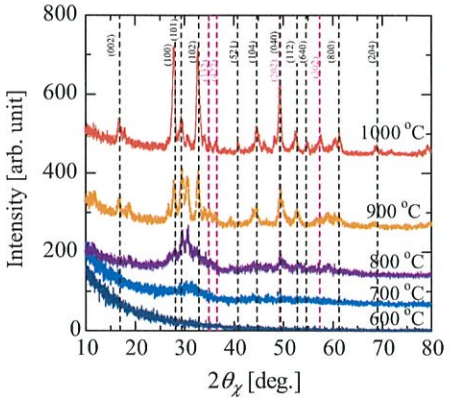

Fig. 11. (Color online.) Effects of thermal annealing on the in-plane XRD patterns of film samples deposited on Si substrates. Black and pink (light gray in b/w) broken vertical lines represent the characteristic diffraction positions of $YAlO_3$ and $Y_3Al_5O_{12}$, respectively.

Curves (a)–(e) in Fig. 12 are the PL emission spectra induced in these five film samples at 10 K. The PL emission spectrum induced in the single crystal plate sample before ion implantation, namely curve I in Fig. 5(b), is again shown for comparison as curve (f). While the films annealed at 600, 700 and 800 °C exhibit no PL, those annealed at 900 and 1000 °C have two or three PL components at about 1.70, 1.75 and 1.80 eV. Here, the peak positions observed in the thermally annealed films differ slightly from those observed in the single crystal plate sample. Regarding this, a very similar phenomenon was observed in $LaAlO_3$ [10]. Namely, the energies of PL components are different between $LaAlO_3$ samples of a bulk shape and of a film shape deposited on a CaF_2 substrate. The authors have already revealed that this difference is due to mismatch in lattice constant between $LaAlO_3$ and the CaF_2 substrate [10]. Therefore, the slight difference in energy between spectrum (f) and spectra (a and b) seems to be due to the difference in lattice constant between $YAlO_3$ and the Si substrate. It is also reasonable that the PL emission spectral curve (a) observed in the film sample annealed at 1000 °C exhibits three components, since the R-line luminescence of Cr^{3+} is composed of two or three components [10,39,41]. Note that the authors could not judge whether the PLs due to oxygen vacancies, Er^{3+}, STEs, and antisites appeared

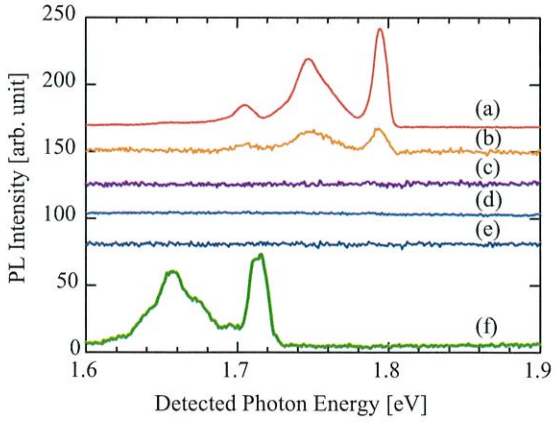

Fig. 12. (Color online.) Comparison among PL emission spectra obtained at 10 K for the unimplanted film samples annealed at 1000 (a), 900 (b), 800 (c), 700 (d) and 600 °C (e) after having been deposited on Si substrates, and the spectrum obtained for the unimplanted single crystal plate sample (f).

or not, due to a very strong PL at around 2–4 eV from the CaF_2 substrate.

The results shown in Figs. 11 and 12 clearly indicate that the PL B due to Cr^{3+} appears only when the sample is crystalline. Namely, the decrease in intensity of the PL B with the two components at 1.66 and 1.71 eV due to Cr^{3+} is not a phenomenon peculiar to the ion implantation. A decrease in PL B should occur similarly to the case shown in Fig. 5(b) when the sample's crystallinity is lowered by any reason. As mentioned above, the PL D at 4.2 eV shown in Fig. 5(c) due to STEs, the PL E at 5.5 eV shown in Fig. 5(d) due to Y^{3+}/Al^{3+} antisites, and the sharp PL A with components at 2.3, 2.6 and 3.1 eV shown in Fig. 5(a) and (c) due to Er^{3+} appear only when the sample's crystallinity is high. Therefore, these PLs disappear when the crystalline structure collapses.

4.4. Comparison with other high permittivity materials

In the authors' previous papers [23,24], the effects of implantation of P^+ or B^+ ions to $LaAlO_3$ and YSZ were reported. While the effect of ion implantation on $LaAlO_3$ is basically very similar to that on $YAlO_3$ reported in the present paper [24], its effect on YSZ, especially on the PL due to oxygen vacancies is quite different [23]. Namely, the PL due to oxygen vacancies in $LaAlO_3$ is scarcely changed by the ion implantation as in the case of PL C in $YAlO_3$. However, the PL due to oxygen vacancies in YSZ decreases its intensity with an increase in fluence of ion implantation. The reason for this is that oxygen vacancies in YSZ do not exist in the form of a structural point defect as in the case of $YAlO_3$ or $LaAlO_3$ [23]. The oxygen vacancies in YSZ exist as a part of its crystal structure to compensate the deficiency of oxygen atoms induced by the stabilization of zirconia by yttria.

5. Conclusions

Single crystal $YAlO_3$ plates were implanted with P^+ or B^+ ions and the resultant changes were analyzed by measuring their optical absorption spectra, in-plane XRD patterns, and PL excitation and emission spectra. Important findings obtained in this work are summarized as follows:

(1) The ion implantation deforms the crystalline structure of $YAlO_3$ and induces localized electronic states in its forbidden band. However, no new PLs are induced.
(2) The PL due to oxygen vacancies is independent of the crystallinity and its intensity is not changed by the ion implantation. On the other hand, the PL due to Cr^{3+} in the ligand field becomes weak by the ion implantation.
(3) Both the PL due to STEs and the one due to Er^{3+} are diminished by the ion implantation. The reason for this is that the exciton states are masked by the localized electronic states induced as a result of the degradation of crystallinity.
(4) The PL due to Y^{3+}/Al^{3+} antisites is also diminished by the ion implantation, since the PL appears only when the sample's crystallinity is high.

Acknowledgments

This research was partly conducted in the UVSOR Facility, Institute for Molecular Science, Okazaki, Japan. It was partly supported by JSPS (Japan Society for the Promotion of Science) Grant 25 3090 for JSPS Fellows. It was also partly supported by the Early Bird Grant, the ENEOS Research Encouragement Prize, and the Mitsubishi Materials Corporation Grant, all from Waseda Research Institute for Science and Engineering.

References

[1] I.F. Elder, M.J.P. Payne, Optics Commun. 148 (1998) 265.
[2] H.Y. Shen, Y.P. Zhou, R.R. Zeng, G.F. Yu, C.H. Huang, Z.D. Zeng, W.J. Zhang, W.X. Lin, Q.J. Ye, J. Appl. Phys. 70 (1991) 3373.
[3] X.M. Duan, B.Q. Yao, G. Li, T.H. Wang, X.T. Yang, Y.Z. Wang, G.J. Zhao, Q. Dong, Laser Phys. Lett. 6 (2009) 279.
[4] M. Moszyński, M. Kapustab, D. Wolskia, W. Klamrac, B. Cederwallc, Nucl. Instrum. Meth. Phys. Res. A 404 (1998) 157.
[5] M. Tardocchi, G. Gorini, A. Pietropaolo, C. Andreani, R. Senesi, N. Rhodes, E.M. Schooneveld, Rev. Sci. Instrum. 75 (2004) 4880.
[6] K. Yasuda, S. Usuda, H. Gunji, Appl. Radiat. Isot. 52 (2000) 365.
[7] S.A. Shevlin, A. Curioni, W. Andreoni, Phys. Rev. Lett. 94 (2005) 146401.
[8] Y.V. Zorenko, A.S. Voloshinovskii, I.V. Konstankevych, Opt. Spectrosc. 96 (2004) 532.
[9] K. Kanai, E. Hirata, Y. Ohki, Jpn. J. Appl. Phys. 47 (2008) 7980.
[10] E. Hirata, K. Tamagawa, Y. Ohki, Jpn. J. Appl. Phys. 49 (2010) 091102.
[11] H. Nishikawa, R. Tohmon, Y. Ohki, K. Nagasawa, Y. Hama, J. Appl. Phys. 65 (1989) 4672.
[12] H. Nishikawa, T. Shiroyama, R. Nakamura, Y. Ohki, K. Nagasawa, Y. Hama, Phys. Rev. B 45 (1992) 586.
[13] H. Nishikawa, R. Nakamura, Y. Ohki, Y. Hama, Phys. Rev. B 48 (1993) 15584.
[14] H. Kato, N. Kashio, Y. Ohki, K.S. Seol, T. Noma, J. Appl. Phys. 93 (2003) 239.
[15] K.S. Seol, T. Watanabe, M. Fujimaki, H. Kato, Y. Ohki, M. Takiyama, Phys. Rev. B 62 (2000) 1532.
[16] T. Morimoto, M. Takase, T. Ito, H. Kato, Y. Ohki, Jpn. J. Appl. Phys. 47 (2008) 6858.
[17] S. Munekuni, T. Yamanaka, Y. Shimogaichi, R. Tohmon, Y. Ohki, K. Nagasawa, Y. Hama, J. Appl. Phys. 68 (1990) 1212.
[18] S. Munekuni, N. Dohguchi, H. Nishikawa, Y. Ohki, K. Nagasawa, Y. Hama, J. Appl. Phys. 70 (1991) 5054.
[19] K.S. Seol, T. Futami, T. Watanabe, Y. Ohki, M. Takiyama, J. Appl. Phys. 85 (1999) 6746.
[20] K.S. Seol, A. Ieki, Y. Ohki, H. Nishikawa, M. Tachimori, J. Appl. Phys. 79 (1996) 412.
[21] H. Kato, A. Masuzawa, H. Sato, T. Noma, K.S. Seol, M. Fujimaki, Y. Ohki, J. Appl. Phys. 90 (2001) 2216.
[22] D. Yamasaka, K. Tamagawa, Y. Ohki, J. Appl. Phys. 110 (2011) 074103.
[23] S. Kaneko, T. Morimoto, Y. Ohki, Jpn. J. Appl. Phys. 54 (2015) 06GC03.
[24] M. Harima, T. Morimoto, Y. Ohki, IEEJ Trans. Electr. Electron. Eng. A 11 (2016).
[25] http://www.srim.org/.
[26] The International Centre for Diffraction Data (ICDD) PDF No. 33–41.
[27] J.F. Ziegler, J.P. Biersack, M.D. Ziegler, SRIM, the Stopping and Range of Ions in Matter, Lulu, 2008, pp. 8–9.
[28] P.D. Townsend, P.J. Chandler, L. Zhang, Optical Effects of Ion Implantation, Cambridge University Press, 2006 (pp. 12, 50, and 82).
[29] F. Lu, M. Huang, F. Yaqoo, M. Lang, F. Namavar, C. Trautmann, H. Sun, R.C. Ewing, J. Lia, Appl. Phys. Lett. 101 (2012) 041904.
[30] J.-H. Lee, I.-H. Choi, S. Shin, S. Lee, J. Lee, C. Whang, S.-C. Lee, K.-R. Lee, J.-H. Baek, K.H. Chae, J. Song, Appl. Phys. Lett. 90 (2007) 032504.
[31] M. Fujimaki, Y. Ohki, H. Nishikawa, J. Appl. Phys. 81 (1997) 1042.
[32] R. Tohmon, Y. Shimogaichi, H. Mizuno, Y. Ohki, Phys. Rev. Lett. 62 (1989) 1388.
[33] K.H. Lee, C. Lofton, K. Kim, W.S. Seo, Y. Lee, M.H. Lee, W. Sigmund, Solid State Commun. 131 (2004) 687.
[34] L. Skuja, J. Non-Cryst. Solids 239 (1998) 16.
[35] H. Nishikawa, E. Watanabe, D. Ito, Y. Ohki, Phys. Rev. Lett. 72 (1994) 2101.
[36] K.S. Seol, Y. Ohki, H. Nishikawa, M. Fujimaki, Y. Hama, J. Appl. Phys. 80 (1996) 6444.
[37] K. Vanheusden, C.H. Seager, W.L. Warren, D.R. Tallant, J.A. Voigt, Appl. Phys. Lett. 68 (1996) 403.
[38] M. Zhu, Z. Zhang, W. Miao, Appl. Phys. Lett. 89 (2006) 021915.
[39] M. Yamaga, H. Takeuchi, T.P.J. Han, B. Henderson, J. Phys. Condens. Matter 5 (1993) 8097.
[40] D. Sugak, A. Matkovskii, D. Savitskii, A. Durygin, A. Suchocki, Y. Zhydachevskii, I. Solskii, I. Stefaniuk, F. Wallrafen, Phys. Status Solidi A 184 (2001) 239.
[41] J. Heber, K.H. Hellwege, S. Leutloff, W. Platz, Z. Phys. 246 (1971) 261.
[42] B. Champagnon, J.H. Høg, Chem. Phys. Lett. 51 (1977) 429.
[43] Ch. Lushchik, E. Feldbach, A. Frorip, M. Kirm, A. Lushchik, A. Maaroos, I. Martinson, J. Phys. Condens. Matter 6 (1994) 11177.
[44] Y.V. Zorenko, A.S. Voloshinovskii, G.M. Stryganyuk, I.V. Konstankevych, Opt. Spectrosc. 96 (2004) 70.
[45] W.L. Yu, J.Z. Wang, Phys. Status Solidi 176 (1993) 433.
[46] M.V. Korzhik, M.G. Livshits, B.I. Minkov, V.B. Pavlenko, Sov. J. Quant. Electron. 22 (1992) 24.
[47] D. Yamasaka, Y. Horii, T. Morimoto, Y. Ohki, Jpn. J. Appl. Phys. 52 (2013) 071501.
[48] C. Duan, P.A. Tanner, V.N. Makhov, M. Kirm, Phys. Rev. B 75 (2007) 195130.
[49] G. Gowda, J. Mater. Sci. Lett. 5 (1986) 1029.